Extruded Monoliths for Gas Separation Processes: Height Equivalent to a Theoretical Plate and Pressure Drop Correlations

AIChE Journal

DOI10.1002/aic.17650

Extruded Monoliths for Gas Separation Processes: Height Equivalent to a Theoretical Plate and Pressure Drop Correlations

Roberto Mennitto, Ishan Sharma and Stefano Brandani*

School of Engineering, University of Edinburgh

The King's Buildings, Mayfield Road

Edinburgh EH9 3BF, U.K.

Abstract

Extruded monoliths are generally adopted in the chemical industry for the advantage of reduced pressure drops at high throughput, but a systematic procedure to evaluate their performance is not readily available. Key performance indicators for a monolith are the Height Equivalent to a Theoretical Plate (HETP) and the pressure drop of its channels. This contribution presents for the first time a systematic approach to the analysis of several extruded monoliths of industrial relevance. A procedure to derive the HETP correlation for an arbitrary extruded monolith is presented, and pressure drop correlations from literature are reviewed. The HETP correlations have been validated against 3D numerical simulations. A reduced-order model is derived from the HETP and is shown to capture the overall dynamics of the 3D simulations with high accuracy without adjustable parameters. Finally, a comparison between the extruded monoliths and packed beds is reported and includes pressure drops.

Keywords: HETP; Pressure Drop; Structured Adsorbent; Extruded Monolith; Process Simulation

***Corresponding author.** E-mail: s.brandani@ed.ac.uk

This article has been accepted for publication and undergone full peer review but has not been through the copyediting, typesetting, pagination and proofreading process which may lead to differences between this version and the Version of Record. Please cite this article as doi: 10.1002/aic.17650
Received: Aug 27, 2021;Revised: Jan 18, 2022;Accepted: Feb 10, 2022

Introduction

In gas separation processes, structured adsorbents can achieve better performance in terms of pressure drop with high gas or liquid velocities and faster cycle times than packed bed adsorption columns[1–4]. Some structured adsorbent applications in gas separation processes are carbon capture[5–7], air separation[8,9], VOC removal[10–12] and desiccant cooling[13,14].

Several types of structured adsorbents have been reported in the literature, such as foams[15,16], fibers[5,17] and laminates[2,18,19], as potential candidates to overcome the limitations of packed beds to handle high flows and good thermal management. Among the different structures, extruded monoliths (EMs) with parallel channels offer the great advantage of extremely low pressure drops. Moreover, channel shape, wall thickness, and cell density can be carefully optimised to enhance the efficiency of EMs in terms of a trade-off between pressure drop and mass transfer rate[20,21]. More recently, additive manufacturing has attracted particular interest as an emerging technology to manufacture monoliths [22–24].

The performance and the design of EMs mainly rely on the definition of the Height Equivalent to a Theoretical Plate (HETP) and pressure drop correlations for the different structures. The HETP is a measure of the solute's dispersion within the EM, and its efficiency. Generally, an ideal monolith is assumed, and a single representative channel analysed as the constitutive element of the structure[25,26]. The equation for the HETP can be seen as the sum of three primary resistances:

$$\frac{HETP}{L} = R_{ax} + R_S + R_v \quad (1)$$

Where the terms on the RHS are: the resistance given by molecular diffusion, R_{ax}, the resistance given by diffusion in the solid, R_S, and the resistance given by the velocity profile in the free cross-section, R_v, respectively.

Taylor[27] first studied the dispersion of a solute inside a channel with no-adsorbing walls and its HETP equation for circular free cross-sections. Aris[28,29] reviewed the work of Taylor and broadened it to elliptical cross-section, and later included also the effect of wall retention in the case of a channel coated with an adsorbent . Moreover, Aris[36] derived the dispersion in a parallel plate geometry and a circular channel as limiting cases for coated channels of annular and elliptical cross-section, respectively.

Golay[26] showed the mathematical approach, based on the analysis of moments, to derive the HETP for rectangular cross-sections. Several other authors have analysed this configuration because of its widespread use in gas and liquid chromatography[25,30,31]. Dutta and Leighton[32–34] replicated the analysis of moments for general cross-sections for chromatographic purposes. They also showed how to split R_v in three independent components namely: $g_1(\alpha)$, $g_2(\alpha)$, $g_3(\alpha)$. The physical meaning of these contributions will be discussed later.

Patton et al.[35] derived the expression of a general linear driving force approximation for the design of an arbitrary monolith. The approximation reduces the monolith's equivalent channel to a hollow cylinder, with the same free cross-sectional area and volume of the solid.

For rectangular cross-sections, Ahn and Brandani[36] pointed out that the resistance given by diffusion in the solid should consider the additional dispersion caused by the solute's diffusion in the corners of the solid to avoid underestimation of the HETP. They proposed a simple approach that redistributes the solid, in the corners of the geometry, to the free cross-section's perimeter, thereby increasing the solid layer's thickness. By definition, this new "corrected thickness" preserves the solid volume in the channel and accounts for the additional dispersion at the corners in the system[36,37].

In terms of pressure drop correlations, the literature provides different correlations for different geometries[4,38,39]. Generally, the flow is assumed laminar in the channel, and the Poisson equation is solved to derive the velocity profile and the pressure drop along the channel[40]. The pressure drop for laminar flow in a channel of an arbitrary, but constant, cross-section is given by:

$$\frac{\Delta P}{L} = \eta v_{ave} \frac{P}{A\Sigma} \frac{fRe_{\Sigma}}{2} \quad (2)$$

Where Σ is a characteristic dimension of the system, and fRe_{Σ} is the Fanning-Reynolds product written with respect to Σ. Generally, the hydraulic diameter, D_h, is used as the characteristic dimension, Σ[41]. As shown by Shah and London[41], this approach leads to different values of the fRe_{D_h} for different channels with the same aspect ratio. Shah and London[41] reported tabulated values of the fRe_{D_h} for a variety of channel shapes. Yilmaz[42] attempted to generalise the approach of Shah and London to derive an equation of fRe_{D_h} for a given channel of arbitrary cross-section. Although the work of Yilmaz[42] is more general than what presented by Shah and London[41] and can be in principle applied to any geometry, the coefficients needed to calculate the fRe_{D_h} are not always easy to derive.

Bahrami et al.[40] developed the analytical solution for the fRe in an elliptical channel whose characteristic length is no longer D_h, but the square root of the cross-sectional area, $\sqrt{A}$. Bahrami et al.[40] showed that the model can be successfully extended to arbitrary cross-sections. Also Muzychka and Yovanovich[43,44] chose $\sqrt{A}$ as characteristic length to derive the "equivalent rectangle model" (ERM) for the calculation of the $fRe_{\sqrt{A}}$. The ERM is based on the analytical solution of the $fRe_{\sqrt{A}}$ for a rectangular channel. The model can be extended to arbitrary geometries through an "effective aspect ratio", as it will be shown in the following.

The ERM has the main advantage to be of simple implementation compared to the models of Bahrami et al.[40] and Yilmaz[42], and it can be used for a variety of cross-sections without the need of tabulated values as for the model of Shah and London[41]. Hence, the pressure drop correlation from Muzychka and Yovanovich[43] can be chosen to be representative of a general correlation for the estimate of pressure drop in an arbitrary monolith.

This paper aims to analyse different EMs of industrial relevance (e.g. honeycomb, triangular and rhombic extruded monolith) and describe their performance in terms of HETP and pressure drop for their single representative channel. The derivations follow the work of Ahn and Brandani on rectangular channels: first R_v is derived for every structure, followed by the redistribution of the solid around the free cross-section to provide R_S. The derived HETP expressions are validated against full 3D simulations. A simplified reduced model, which captures the overall dynamics of 3D simulations with high accuracy, is also derived from the HETP. It is followed by a brief overview of the pressure drop correlation proposed by Yovanovich and co-workers. The pressure drop correlation, and the HETP are used to compare EMs and conventional packed beds.

Geometries of interest

The geometries analysed are shown in Fig.1. They take into account several shapes that are commonly found in industrial applications. They have been split into two categories: flat and rounded geometries. “Flat” geometries are those where the solid diffusion can be approximated as the diffusion in a slab. “Rounded” geometries are those where the diffusion in the solid can be approximated by the diffusion in a hollow cylinder.

As discussed in the introduction, the rectangular and hollow cylinder have been already studied in great detail and are reported for completeness.

The study of the triangular channel is limited to isosceles ones. Indeed, an isosceles triangle can be seen as the single representative channel of an ideal EM. It is evident that the study of irregular triangles would have very limited relevance for practical applications.

Two forms of the honeycomb monolith have been considered: the hexagonal free cross-section and the circular free cross-section. The circular cross-section can be seen as a realistic representation of a honeycomb monolith where the adsorbent is deposited as a coating. The ideal hexagonal channel represents a monolith extruded directly using the adsorbent material. The hexagonal channel with circular cross-section will be denoted as "hex-cir" channel, and the hexagonal free cross-section one as "hex-hex" channel. For the hex-cir channel, only the regular hexagon will be investigated. Indeed, coatings of non-regular hexagonal channels might result in non-uniform free cross-sections that would require specific analysis and not general correlations, which are the main aim in this work. To define the geometry of the hex-hex channel two parameters are needed. Here two aspect ratios are used, starting from the inner rectangle of aspect ratio $\alpha_{rec} = \frac{i_{rec}}{h}$, and two triangles are attached either on the short side or on the long sides. If the triangles are attached on the short sides, the second aspect ratio is defined as $\alpha_{ss} = \frac{i_{ss}}{i_{rec}}$. If the triangles are attached on the long sides, the second aspect ratio is defined as $\alpha_{ls} = \frac{i_{ls}}{h}$. The values of the aspect ratios for a hex-hex channel with a regular hexagonal free cross-section are $\alpha_{rec} = \frac{1}{\sqrt{3}}$, $\alpha_{ls} = \frac{1}{2\sqrt{3}}$.

The aspect ratio for the other geometries has been defined as $\alpha = i/h$, where h and i are the characteristic dimensions of the geometry highlighted in Fig.1. All the geometries have been studied with the same approach proposed by Ahn and Brandani[36]. A schematic diagram of the

procedure used in the analysis of the different channels can be seen in Fig.2. Applying the solid redistribution of Ahn and Brandani[36], a "corrected" thickness of the solid, R_S can be established. The analysis of the moments presented by Dutta and Leighton[33] can be used to derive expressions for the different contributions to the resistance R_v. The remaining resistance, R_{ax}, can be directly estimated from the molecular diffusivity of the solute and average velocity inside the channel, as in eq.(3). The new HETP expression for a given channel has been validated against 3D simulations. Finally, a simplified reduced model, capturing the overall dynamics of the 3D simulations, has been derived from the HETP.

HETP for an arbitrary cross-section

Generally, the HETP for an isothermal, linear system and flat geometry (grey in Fig.1) is given by[29]

$$HETP = 2\frac{D_m}{v_{ave}} + \frac{2k}{3(1+k)^2}\frac{w^2}{D_s}v_{ave} + C_M\frac{h^2}{D_m}v_{ave} \quad (3)$$

The term C_M depends only on the geometry and, consequently, on the velocity profile. C_M can be written as[33]

$$C_M = \frac{1}{6}\left(\frac{k}{1+k}\right)^2 g_1(\alpha) + \frac{1}{105}g_2(\alpha) + \frac{1}{15}\left(\frac{k}{1+k}\right)g_3(\alpha) \quad (4)$$

where $k = (1-\epsilon)K/\epsilon$. The function $g_1(\alpha)$ quantifies the effect of wall retention with a uniform flow in the free cross-section, $g_2(\alpha)$ accounts for the resistance given by the flow in the same channel with non-adsorbing walls, and $g_3(\alpha)$ quantifies the interaction between the previous two functions.

For rounded geometries, the free cross-section's curvature must be taken into account when writing the expression of the HETP. Aris[28] derived the analytical expression of the HETP for a hollow cylinder[45,46] given by

$$HETP = 2\frac{D_m}{v_{ave}} + \frac{2f_1 k}{(1+k)^2}\frac{\left(2Rw+w^2\right)}{D_s}v_{ave} + C_M\frac{d^2}{D_m}v_{ave} \quad (5)$$

where

$$f_1 = \frac{\frac{2p^4\ln(p^2)}{p^2-1}-(3p^2-1)}{8(p^2-1)} \quad (6)$$

given $p = \frac{R+w}{R}$. For circular geometries, the dispersivity coefficient can be written as[29,45,46]

$$C_M = \frac{1+6k+11k^2}{96(1+k^2)} \quad (7)$$

Derivation of the $g_i(\alpha)$ functions

The procedure to derive $g_i(\alpha)$ is the same as that reported by Dutta and Leighton[32]; the procedure is valid for any arbitrary cross-section. The integro-differential equations reported in the Supplementary Information are solved using COMSOL Multiphysics 5.1 to obtain the $g_i(\alpha)$ functions. The numerical methodology was validated using the rectangular geometry and the analytical expressions derived by Ahn and Brandani[36] (see Supplementary Information).

To provide a simple design relationship, the $g_i(\alpha)$ values for triangular and rhombic are fitted with the correlations in eq.(8a) and eq.(8b):

$$g_i(\alpha) = \frac{j_{1i}\alpha^5+j_{2i}\alpha^4+j_{3i}\alpha^3+j_{4i}\alpha^2+j_{5i}\alpha+j_{6i}}{\alpha^3+s_{1i}\alpha^2+s_{2i}\alpha+s_{3i}} \quad \text{for triangular} \quad (8a)$$

$$g_i(\alpha) = j_{1i}\alpha^{j_{2i}} + j_{3i}\alpha^{j_{4i}} + j_{5i} \quad \text{for rhombic} \quad (8b)$$

$$g_i(\alpha) = \frac{j_{1i}(\alpha+j_{2i})^2}{(\alpha+j_{3i})^2} + j_{4i} \qquad \text{for rectangular} \qquad (8c)$$

where $\alpha \in [0.175;11.34]$ for the triangular channel and $\alpha \in [0.05;1]$ for the rhombic channel. The correlated parameters are reported in Supplementary Material, and the results for triangular and rhombic channels are plotted in Fig.3. Care must be taken when eq.(8) is used to derive the values of $g_i(\alpha)$ for the geometries presented. Indeed, eq.(8) is only valid in the range of aspect ratios analysed, which would also represent practical EMs. In eq.(8c) the correlation derived for a rectangular channel from Ahn and Brandani[36] is reported. The correlation for the rectangular channel is valid for any arbitrary aspect ratio between 1 and ∞.

The results for the hex-hex channel are presented in Fig.4. The more the cross-section approaches the regular hexagon the lower will be the dispersion. The correlation for the $g_i(\alpha)$ functions of the hex-hex channel are reported in the supplementary material. The range of aspect ratios analysed is: $\alpha_{rec} \in [0.25;1]$, $\alpha_{ls} \in [0;2.5]$ and $\alpha_{ss} \in [0;2.83]$.

Correlations for the corrected thickness

To obtain R_S, the corrected wall thickness for each geometry needs to be specified. This is of particular importance since Ahn and Brandani[36] showed that the diffusion in the solid often gives the main resistance in gas separation processes.

The corrected thickness represents a redistribution of the solid from the corners of the geometry to the free cross-section's perimeter. The correction aims to reduce the 2D diffusion problem in the solid cross-section to a 1D diffusion problem. The redistribution also preserves

the total amount of solid around the geometry. A visual representation is shown in Fig.5 for both triangular (flat) and hex-cir (rounded) channels. In a triangular channel, the solute first travels from the fluid phase to the grey region of the solid, perpendicular to its perimeter. Then, the molecules diffuse through the corners in both vertical and horizontal directions. By redistributing the solid, the solute's diffusion is approximated as a 1D diffusion problem, perpendicular to the perimeter. Equivalent considerations can be made for the hex-cir channel (Fig.5b).

For flat geometries, a mathematical form to express the corrected thickness is:

$$w_c = \frac{A_S}{P} \tag{9}$$

where A_S is the area occupied by the solid at the cross-section, and P is the perimeter of the free cross-section.

Analytical expressions for w_c can be derived from the equation above as a function of the system's characteristic length. For rounded geometries, the corrected thickness has to be calculated from eq.(10), which equates the area of the solid around the channel, A_S, to the area of the solid surrounding a hollow cylinder with the same free cross-section:

$$w_c = \frac{\sqrt{\frac{4A_S}{\pi}+d^2}-d}{2} \tag{10}$$

Where d is the diameter of the free circular cross-section (Fig.5). The equation above maintains a constant volume of solid around the free circular cross-section. Eq.(9) would lead to a different volume of solid if applied to rounded geometries, violating the conservation of the mass of solid around the free cross-section during the redistribution. Table 1 provides the

equations to calculate the corrected thickness of the different geometries under analysis. The procedure to derive the corrected thickness for an arbitrary hex-hex channel is reported in Table 2.

Having defined the corrected thickness, R_S can be calculated, i.e. the second term of eq.(3) or (5), where w_c replaces w. The HETP correlations are therefore completely defined for all the geometries of interest. For the validation of these correlations, 3D numerical simulations of the different channels are reported next.

3D Numerical model

For the 3D model, a single representative channel of the monolith is considered. The reference system considers the cross-section of the monolith on the xy-plane and the length of the channel along the z-axis. The main assumptions of the 3D model are as follows:

- Isothermal conditions
- Linear isotherm
- Trace component system
- Fully-developed laminar flow in the channel
- Negligible pressure drop along the channel
- Negligible axial (z-axis) diffusion in the solid
- Equilibrium at the fluid-solid interface

The assumption of negligible pressure drops is close to the realistic behaviour of EMs. The full set of material balance equations are reported in the Supplementary Information.

The average outlet concentration in the fluid phase is calculated using eq. (11).

$$c_{ave}|_{L,t} = \frac{\oiint v_{(x,y)} c|_{L,t} dxdy}{\oiint v_{(x,y)}\, dxdy} \quad (11)$$

μ is the first moment of the breakthrough curve, i.e. its mean residence time, and can be calculated from an integral mass balance on the system:

$$\mu = \frac{L}{v_{ave}}\left[1 + \frac{1-\epsilon}{\epsilon} K\right] \quad (12)$$

The velocity profile inside the channel is governed by the Navier-Stokes equations in steady-state viscous flow, with no-slip boundary conditions at the fluid-solid interface. The flow is assumed to be fully developed at the free cross-section's inlet for all the simulations. This assumption arises from the fact that the entry length for a gas flowing in a channel is orders of magnitude shorter than the column length. The entry length can be estimated as $L_{entry} \approx C_0 Re D_h$[43], where $C_0 \in [0.01, 0.06]$, $Re \in [0.1, 50]$ and $D_h \sim 0.001\, m$ for most practical applications. These values give an $L_{entry} \sim 0.001\, L_{column}$.

The 3D numerical code has been validated against the results from Ahn and Brandani[36], based on the analytical solution of the velocity profile in a rectangular channel of arbitrary aspect ratio.

The physical parameters used for both 3D and reduced model simulations are listed in Table 3. The parameters refer to a CO_2/N_2 system where the solid is a carbon monolith[36].

The dimensionless set of equations for the 3D model has been solved using the finite-element method in COMSOL Multiphysics 5.1. The integration limit of the simulation was set to twice the first moment of the system. The mesh consisted of triangular prismatic elements in both

fluid and solid domains. Furthermore, a mesh-refinement study has also been conducted to ensure that the results are not dependent on the chosen mesh size. An example of mesh refinement is reported in the supporting material.

From the breakthrough curve, the values of the first and second moment can be defined as:

$$1^{st}\ Moment\ \ \mu = \int_0^{\infty} \frac{c}{c_{in}} dt \tag{13}$$

$$2^{nd}\ Moment\ \ \sigma^2 = 2\int_0^{\infty} \frac{c}{c_{in}} t\ dt - \mu^2 \tag{14}$$

Since the second moment is strongly affected by numerical oscillations, an exponential function of the form ae^{-bt}, has been used to approximate the tail of the breakthrough curve[47]. Hence:

$$2^{nd}\ Moment\ \ \sigma^2 = 2\int_0^{t_0} \frac{c}{c_{in}} t\ dt + 2\frac{a}{b} e^{-bt_0}\left(t_0 + \frac{1}{b}\right) - \mu^2 \tag{15}$$

where, t_0 is the starting time of the exponential decay.

Finally, the HETP is calculated from the following equation:

$$\frac{HETP}{L} = \frac{\sigma^2}{\mu^2} \tag{16}$$

Once the 3D model has been validated using a hollow fiber geometry (see Supplementary Information), the comparison between 3D simulations and HETP predictions can be made, as shown in Fig.6. There is an excellent match between the predicted HETP from eq.(3) and eq.(5) with the HETP calculated from 3D simulations for all the geometries analysed. It should be noted how the fluid resistance, the sum of molecular diffusion and velocity profile resistances, only play a small role in the total spreading of the breakthrough curve. The transversal diffusion of the solute in the free cross-section immediately decreases the

dispersion caused by the velocity profile, leading to a near plug flow inside the free channel. This behaviour has been observed in all the 3D simulations carried out. Indeed, the ratio between characteristic times for convection and diffusion along a cross-section, $\frac{LD_m}{vh^2}$, is generally higher than 1 for gas separations, which explains the homogeneous concentration profile at a given cross-section in the channel. Hence, in most gas systems, the optimisation of an arbitrary geometry to decrease the dispersion caused by the velocity profile would only lead to minor improvements in the monolith's performance. Particular effort should be aimed at reducing the mass transfer resistance in the solid, R_s in eq.(1), which is the leading cause of dispersion in the HETP equation.

Reduced model for channel dynamics

While the use of the full solution to the 3D model can be used to study a single channel's dynamic response, it is computationally demanding. It is therefore important to be able to approximate the breakthrough response using a model of reduced dimensionality. Hereafter this will be referred to as the reduced model, where 1D is assumed along the channel's axis for the fluid, and 1D for the solid in a direction perpendicular to the channel axis. The full set of modelling equations are included in the Supplementary Information.

The reduced model has been solved in gPROMS with the method of lines, using orthogonal collocation on finite elements to discretise both the fluid and solid domains. The spatial discretisation has been refined gradually in order to provide results independent from the number of elements used. The thickness of the solid domain has been set equal to the simulated geometry's corrected thickness. It should be noted that the reduced model does not include any adjustable parameter.

Fig.6 shows the HETP values calculated from the different approaches, confirming that the reduced model (blue circles) is in excellent agreement with the 3D simulations (red squares). For the triangular and hex-hex geometries the predictions from the model presented by Patton et al.[35] are also included, showing considerable deviation. In this case, the reduced model includes the effective terms from the equivalent hollow cylinder and R_S is calculated according to the LDF approximation presented by Patton et al.[35]. The deviation from the 3D simulations can be attributed to two main reasons: the approximation of the channel to a hollow cylinder, and the change in the channel's porosity. The former is important particularly for the triangular geometry, as the diffusion process in the triangular channel is substantially different from the one of a hollow cylinder, where the curvature of the geometry has to be taken into account. The latter is important for both geometries and is a consequence of preserving the surface area and volume of the solid. In the hex-hex channel the capacity is reduced by 10% and a thinner diffusive length is predicted using the correlation of Patton et al.[35]. This leads to a much lower HETP compared to 3D simulations. With the use of the corrected thickness the volume of the solid and the volume of the free channel are preserved, keeping the porosity the same as the original system. The preservation of the surface area of the cross-section, rather than its volume, leads to a decrease in the triangular channel's porosity in Fig.6 by almost 40%, which explains the sharp increase of the HETP compared to the 3D simulations.

It could be argued that the hex-hex channel should be treated as a flat geometry, and consequently eq.(3) to be used to calculate its HETP. It should be noted that, as the number of sides in a polygon increases, the hollow cylinder limit is approached. The hex-hex channel approximates the shape of a hollow cylinder, for which eq.(5) holds for the HETP. Furthermore, the HETP for a hollow cylinder, eq.(5), tends to the HETP for a flat geometry,

eq.(3), for thin films of solid around the free cross-section, as shown by Schisla and Carr[46]. Hence, eq.(5) can be used regardless of the thickness of the solid around the cross-section.

Fig.7 compares the breakthrough curves obtained from the full 3D simulations and the reduced model. The values of $\frac{v_{ave}L}{D_m}$ for each simulation are reported in the supporting material. The use of an effective axial dispersion to account for the effect of the fluid velocity profile, and the effective thickness to account for the additional resistance to mass transport in the corners, results in a reduced model that captures the key physical behaviour, giving an excellent agreement. The size of the numerical problem, and hence the computational time, is more than an order of magnitude smaller for the reduced model. The reduced model serves as an effective tool for fast screening of EMs for different separation processes.

Pressure Drop Correlation

Dispersion within the channel is not the only parameter to assess an EM's performance for a given separation. Pressure drops are crucial to evaluate the energy penalty of a separation process, especially at high throughput. In this section, a brief overview of the ERM model developed by Muzychka and Yovanovich[43] is presented.

Firstly, to calculate the pressure drop in a channel, the "effective" aspect ratio has to be defined according to Table 4.

Then, $fRe_{\sqrt{A}}$ can be calculated using

$$fRe_{\sqrt{A}} = \frac{12}{\sqrt{\gamma}(1+\gamma)\left[1-\frac{192\gamma}{\pi^5}\tanh\left(\frac{\pi}{2\gamma}\right)\right]} \quad (17)$$

The validity of this relationship for hex-hex channels has been checked numerically solving the Navier-Stokes equations in COMSOL for each channel. The results are as shown in Fig.8.

In the case where the effective aspect ratio is 1, $fRe_{\sqrt{A}} = 14.23$. The main benefit of using this approach is that this constant value is applicable to the vast majority of industrially relevant channels (regular polygons and circular cross-section). The approach of using the hydraulic diameter as characteristic length would have led to different values of fRe_{D_h} for every channel even for $\alpha = 1$. Moreover, each channel would require a separate equation to describe the fRe_{D_h} for $\alpha \neq 1$.

Coupling eq.(2) and (18) the average velocity and the pressure drop across the monolith can be calculated

$$F = N_C v_{ave} A \quad (18)$$

Ahn and Brandani[31] have shown how to generalize eq.(18) in case of a real monolith comprising of slightly dissimilar channels, assuming a distribution of channel sizes. The slightly different channel sizes[31,49], wall thicknesses[31], and flow mal-distributions[21] also cause additional dispersion in the breakthrough curve.

Comparison between packed bed and monoliths

In what follows, a comparison between EMs and a packed bed is presented. The analysis is based on their respective pressure drop per theoretical stage. The derivation follows the approach of Ruthven and Thaeron[2] for a parallel passage contactor.

For a packed bed the Ergun equation is used for the pressure drop, with the assumption that the particles are small enough to neglect turbulent contributions:

$$\frac{\Delta P_{Packed}}{L} = 37.5\eta \frac{\epsilon_p v}{R_p^2} \frac{\left(1-\epsilon_p\right)^2}{\epsilon^3} \quad (19)$$

For the HETP we assume that $K \gg \epsilon$:

$$\frac{HETP_{Packed}}{L} = \frac{2\epsilon_p D_{ax}}{\epsilon_p v} + \frac{2}{15} \frac{\epsilon_p v}{(1-\epsilon_p)K} \frac{R_p^2}{D_s} \quad (20)$$

Under these conditions, the axial dispersion in the packed bed becomes $D_{ax} \approx 0.7 D_m$[50].

Equations (2), (3), (19) and (20) can now be used to derive the ratio of the pressure drop per theoretical stage, $R\left(\frac{D_m}{\epsilon_p v R_p}, \frac{D_m}{KD_s}\right) = \left(\Delta P \times \frac{HETP}{L}\right)_{packed\ bed} / \left(\Delta P \times \frac{HETP}{L}\right)_{EM}$, and the full details can be found in the Supplementary Information.

EMs generally exhibit a lower pressure drop per theoretical stage. Therefore, monoliths with flat cross-sections show less pressure drop per number of stages compared to a packed bed under all practical conditions. The function $R\left(\frac{D_m}{\epsilon_p v R_p}, \frac{D_m}{KD_s}\right)$ is monotonic with respect to its variables and as a result a simple comparison is obtained from the limiting values reported in Table 5.

Note that

$$\lim_{\frac{D_m}{KD_s} \to 0^+} R\left(\frac{D_m}{\epsilon_p v R_p}, \frac{D_m}{KD_s}\right) = \lim_{\frac{D_m}{\epsilon_p v R_p} \to \infty} R\left(\frac{D_m}{\epsilon_p v R_p}, \frac{D_m}{KD_s}\right) \quad (21)$$

and

$$\lim_{\frac{D_m}{KD_s}\to\infty} R\left(\frac{D_m}{\epsilon_p v R_p},\frac{D_m}{KD_s}\right) = \lim_{\frac{D_m}{\epsilon_p v R_p}\to 0+} R\left(\frac{D_m}{\epsilon_p v R_p},\frac{D_m}{KD_s}\right) \quad (22)$$

Conclusions

Simple analytical correlations for HETP and pressure drop of several extruded monoliths of industrial relevance have been derived for the first time. The analytical correlations can be used to calculate the HETP for aspect ratios of practical relevance. The main advantage of the HETP correlation for a given monolith is twofold: a simple yet reliable tool for the preliminary design of the EM, and an accurate breakdown of the different resistances that affect the performance of the EM under analysis. The resistance due to the molecular diffusivity, velocity profile, and solid diffusion have been quantified for the EMs analysed. The corrected thickness approach has been shown to be applicable to all geometries considered and the resulting HETP expression has been validated against full 3D numerical simulations. The mass transfer in the solid caused the maximum dispersion in the system for all the cases studied. This is of key importance in the optimisation of EMs, as it highlights the relative importance of minimising the diffusion resistance in the solid, rather than the minimisation of the dispersion in the gas phase.

From the HETP correlation, a reduced model has been developed with the aim of providing a fast and reliable tool to capture the overall dynamics of the 3D simulations. The reduced model considers 1D along the axis of the channel, and 1D for the diffusion in the solid. The reduced model predicts the same breakthrough dynamics as the full 3D simulations at a very small fraction of the computational cost. It thus provides a very useful tool for the optimization of adsorption processes that use extruded monoliths for different separation

purposes. The parameters of the reduced model are all predicted from the geometry and the physical properties of the system under analysis.

Pressure drop correlations for such channels were also reviewed. The HETP and pressure drop correlations were combined to compare EMs to conventional packed beds obtaining the respective pressure drops per theoretical stage. This comparison shows that the monoliths perform better than packed beds under all practical conditions, proving that monoliths can be an important tool in process intensification and for the deployment of fast-cycle adsorption processes limited by the energy penalty associated with large pressure drops.

Acknowledgements

Financial support from the Engineering and Physical Sciences Research Council, under the grant Versatile Adsorption Processes for the Capture of Carbon Dioxide from Industrial Sources – FlexICCS (EP/N024613/1), is gratefully acknowledged.

Nomenclature

a	Fitting parameter of the exponential decay (mol m^{-3})
A	Free cross-sectional area (m^2)
A_S	Solid area (m^2)
b	Fitting parameter of the exponential decay (s^{-1})
c	Fluid concentration (mol m^{-3})
$c_{ave}\|_{L,t}$	Average outlet concentration (mol m^{-3})
C_M	Taylor-Aris dispersivity coefficient (-)
d	Diameter of the circular cross-section (m)

D_m	Molecular diffusion ($m^2\ s^{-1}$)
D_s	Diffusion in the solid ($m^2\ s^{-1}$)
f_1	Aris' curvature factor (-)
fRe	Fanning-Reynolds product (-)
F	Flowrate ($m^3\ s^{-1}$)
$g_1(\alpha)$	Effect of wall retention with a uniform flow in the free cross-section
$g_2(\alpha)$	Resistance given by the flow in a channel with no adsorbing walls
$g_3(\alpha)$	Interaction term between $g_1(\alpha)$ and $g_2(\alpha)$
h	Characteristic length in the y-axis direction of a cross-section (m)
i	Characteristic length in the x-axis direction of the free cross-section (m)
i_{rec}	Smallest dimension of the rectangle in hex-hex channel (m)
i_{ls}	Height of the triangle for the hex-hex channel when $\alpha_{ss} = 0$ (m)
i_{ss}	Height of the triangle for the hex-hex channel when $\alpha_{ls} = 0$ (m)
k	Partition coefficient (-)
K	Henry's law constant (-)
L	Length of the monolith (m)
N_C	Number of channels (-)

p	Ratio of outer and inner diameter of a circular coated channel (-)
P	Perimeter of the free cross-section (m)
R	Inner diameter of the hollow fiber (m)
R_{ax}	Axial dispersion resistance (-)
R_p	Radius of the particle in the packed bed (m)
R_S	Resistance given by the diffusion in the solid (-)
R_v	Resistance given by the velocity profile (-)
t	Time (s)
t_0	Initial time of the exponential decay (s)
$v_{(x,y)}$	Velocity (m s^{-1})
v_{ave}	Average velocity (m s^{-1})
w	Thickness of the solid (m)
w_c	Corrected thickness of the solid (m)
x, y	Coordinates on the cross-section
z	Axial coordinate
Greek letters	
α	Aspect ratio (-)
γ	Effective aspect ratio (-)
ΔP	Pressure drop (Pa)

ϵ	Bed void fraction (-)
ϵ_p	Void fraction of the packed bed (-)
η	Viscosity (Pa s)
μ	Mean residence time (s)
σ	Square root of the second moment (-)
Σ	Characteristic length for the pressure drop (m)

References

1. Ruthven DM. Past Progress and Future Challenges in Adsorption Research. *Ind Eng Chem Res*. 2000;(39):2127-2131.

2. Ruthven DM, Thaeron C. Performance of a parallel passage adsorbent contactor. *Gas Sep Purif*. 1996;10:63-73.

3. Rezaei F, Webley P. Structured adsorbents in gas separation processes. *Sep Purif Technol*. 2010;70(3):243-256.

4. Rezaei F, Webley P. Optimum structured adsorbents for gas separation processes. *Chem Eng Sci*. 2009;64(24):5182-5191.

5. Fan Y, Kalyanaraman J, Labreche Y, et al. CO_2 Sorption performance of composite polymer/aminosilica hollow fiber sorbents: An experimental and modeling study. *Ind Eng Chem Res*. 2015;54(6):1783-1795.

6. Zhao Q, Wu F, Men Y, et al. CO_2 capture using a novel hybrid monolith (H-ZSM5/activated carbon) as adsorbent by combined vacuum and electric swing adsorption (VESA). *Chem Eng J*. 2019;358:707-717.

7. Sharma I, Friedrich D, Golden T, Brandani S. Monolithic Adsorbent-Based Rapid-Cycle Vacuum Pressure Swing Adsorption Process for Carbon Capture from Small-Scale Steam Methane Reforming. *Ind Eng Chem Res*. 2020;59(15):7109-7120.

8. Nevell JM, Perera SP. Novel adsorbent hollow fibres for oxygen concentration. *Adsorption*. 2011;17(1):273-283.

9. Kopaygorodsky EM, Guliants V V., Krantz WB. Predictive Dynamic Model of Single-Stage Ultra-Rapid Pressure Swing Adsorption. *AIChE J*. 2004;50(5):953-962.

10. Maldonado-Hódar FJ, Moreno-Castilla C, Carrasco-Marín F, Pérez-Cadenas AF. Reversible toluene adsorption on monolithic carbon aerogels. *J Hazard Mater*. 2007;148(3):548-552.

11. Wang S, Bai P, Wei Y, et al. Three-Dimensional-Printed Core-Shell Structured MFI-Type Zeolite Monoliths for Volatile Organic Compound Capture under Humid Conditions. *ACS Appl Mater Interfaces*. 2019;11(42):38955-38963.

12. Lee LY, Perera SP, Crittenden BD, Kolaczkowski ST. Manufacture and Characterisation of Silicalite Monoliths. *Adsrption Sci Technol*. 2000;18:147-170.

13. Brandani F, Rouse A, Brandani S, Ruthven DM. Adsorption Kinetics and Dynamic Behavior of a Carbon Monolith. *Adsorption*. 2004;10:99-109.

14. Cheng D, Peters EAJFF, Kuipers JAMH. Performance study of heat and mass transfer in an adsorption process by numerical simulation. *Chem Eng Sci*. 2017;160:335-345.

15. Gargiulo N, Caputo D, Totarella G, Lisi L, Cimino S. Me-ZSM-5 monolith foams for the NH_3 -SCR of NO. *Catal Today*. 2018;304:112-118.

16. Lee BY, Lee JS, Park YS. Synthesis of Large Monolithic Zeolite Foams with Variable Macropore Architectures. *Adv Mater*. 2001;13(16):1259-1263.

17. Rezaei F, Subramanian S, Kalyanaraman J, Lively RP, Kawajiri Y, Realff MJ. Modeling of rapid temperature swing adsorption using hollow fiber sorbents. *Chem Eng Sci*. 2014;113:62-76.

18. Narayanan S. Laminate Zeolite Structure prepared using Papermaking Techniques for Carbon Dioxide Capture : Synthesis , Characterisation and Performance. 2014; PhD Thesis, Monash University.

19. He B, Liu J, Zhang Y, Zhang S, Wang P, Xu H. Comparison of structured activated carbon and traditional adsorbents for purification of H_2. *Sep Purif Technol*. 2020;239(5):116529.

20. Rezaei F, Mosca A, Hedlund J, Webley PA, Grahn M, Mouzon J. The effect of wall porosity and zeolite film thickness on the dynamic behavior of adsorbents in the form of coated monoliths. *Sep Purif Technol*. 2011;81(2):191-199.

21. Sharma I, Mennitto R, Friedrich D, Brandani S. Combining the Nonuniform Structure and Flow Maldistribution for the Accurate Prediction of the Process Performance of Monolithic Adsorbent Systems. *Ind Eng Chem Res*. 2020;59(7):3162-3172.

22. Thakkar H, Eastman S, Hajari A, Rownaghi AA, Knox JC, Rezaei F. 3D-Printed Zeolite Monoliths for CO2 Removal from Enclosed Environments. *ACS Appl Mater Interfaces*. 2016;8(41):27753-27761.

23. Regufe MJ, Ferreira AFP, Loureiro JM, Rodrigues A, Ribeiro AM. Electrical conductive 3D-printed monolith adsorbent for CO_2 capture. *Microporous Mesoporous Mater*. 2019;278(October 2018):403-413.

24. Claessens B, Dubois N, Lefevere J, Mullens S, Cousin-Saint-Remi J, Denayer JFM. 3D-Printed ZIF-8 Monoliths for Biobutanol Recovery. *Ind Eng Chem Res*. 2020;59(18):8813-8824.

25. Spangler GE. Height equivalent to a theoretical plate theory for rectangular GC columns. *Anal Chem*. 1998;70(22):4805-4816.

26. Golay MJE. Theory of Chromatography in Open and Coated Tubular Columns with Round and Rectangular Cross-Sections. In: Coates VJ, Noebles HJ, Fagerson IS, eds. *Gas*

Chromatography. New York: Academic Press; 1958:1-13.

27. Taylor GI. Diffusion and Mass Transport in Tubes. *Proc Phys Soc Sect B*. 1954;67(12):857-869.

28. Aris R. On the dispersion of a solute by diffusion, convection, and exchange between phases. *Proc R Soc Lond*. 1959;252:538-550.

29. Aris R. On the dispersion of a solute in a fluid flowing through a tube. *Proc R Soc London*. 1956;A235(1298):67-77.

30. Gritti F, Piatkowski W, Guiochon G. Study of the mass transfer kinetics in a monolithic column. *J Chromatogr A*. 2003;983(1-2):51-71.

31. Ahn H, Brandani S. Dynamics of Carbon Dioxide Breakthrough in a Carbon Monolith Over a Wide Concentration Range. *Adsorption*. 2005;11:473-477.

32. Dutta D, Leighton DT. Dispersion Reduction in Open-Channel Liquid Electrochromatographic Columns via Pressure-Driven Back Flow. *Anal Chem*. 2003;75(14):3352-3359.

33. Dutta D, Leighton DT. Dispersion in Large Aspect Ratio Microchannels for Open-Channel Liquid Chromatography. *Anal Chem*. 2003;75(1):57-70.

34. Dutta D, Leighton DT, Ramachandran A. Effect of channel geometry on solute dispersion in pressure-driven microfluidic systems. *Microfluid Nanofluid*. 2006;2:275-290.

35. Patton A, Crittenden BD, Perera SP. Use of the linear driving force approximation to guide the design of monolithic adsorbents. *Chem Eng Res Des*. 2004;82(8):999-1009.

36. Ahn H, Brandani S. Analysis of breakthrough dynamics in rectangular channels of arbitrary aspect ratio. *AIChE J*. 2005;51(7):1980-1990.

37. Yan X, Liu M, Zhang J, Zhu H, Li Y, Liang K. On-chip investigation of the hydrodynamic dispersion in rectangular microchannels. *Microfluid Nanofluidics*. 2015;19(2):435-445.

38. Shah RK, London AL. *Laminar Flow Forced Convection in Ducts*. New York: Academic Press; 1978.

39. Cybulski A, Moulijn JA. *Structured Catalysts and Reactors*. Boca Raton: CRC; 1998.

40. Bahrami M, Yovanovich MM, Culham JR. A novel solution for pressure drop in singly connected microchannels of arbitrary cross-section. *Int J Heat Mass Transf*. 2007;50(13-14):2492-2502.

41. Shah RK. Laminar flow friction and forced convection heat transfer in ducts of arbitrary geometry. *Int J Heat Mass Transf*. 1975;18:849-862.

42. Yilmaz T. General Equations for Pressure Drop for Laminar Flow in Ducts of Arbitrary Cross Sections. *J Energy Resour Technol Trans ASME*. 1990;112(4):220-223.

43. Muzychka YS, Yovanovich MM. Pressure Drop in Laminar Developing Flow in Noncircular Ducts : A Scaling and Modeling Approach. *J Fluids Eng*. 2009;131(11):1-11.

44. Muzychka YS, Yovanovich MM. Laminar forced convection heat transfer in the combined entry region of non-circular ducts. *J Heat Transfer*. 2004;126(1):54-61.

45. Schisla DK, Ding H, Carr PW, Cussler EL. Polydisperse tube diameters compromise multiple open tubular chromatography. *AIChE J*. 1993;39(6):946-953.

46. Schisla DK, Carr PW. Limitations of the Assumption of Negligible Film Thickness in

Capillary Chromatography. *Chromatographia*. 1990;29(11-12):606-608.

47. Brandani S, Ruthven DM. Moments Analysis of the Zero Length Column Method. *Ind Eng Chem Res*. 1996;35(1):315-319.

48. Duan Z, Yovanovich MM. Models for Gaseous Slip Flow in Circular and Noncircular Microchannels. In: *Proceedings of FEDSM-ICNMM2010-30320, Montreal, Canada, August 1-5*. ; 2010:1-11.

49. Crittenden BD, Camus O, Perera SP, et al. Nonuniform Channels in Adsorbent Monoliths. *AIChE J*. 2011;57(5):1163-1172.

50. Langer G, Roethe A, Roethe KP, Gelbin D. Heat and mass transfer in packed beds-III. Axial mass dispersion. *Int J Heat Mass Transf*. 1978;21(6):751-759.

AIChE Journal

DOI10.1002/aic.17650

List of Figures

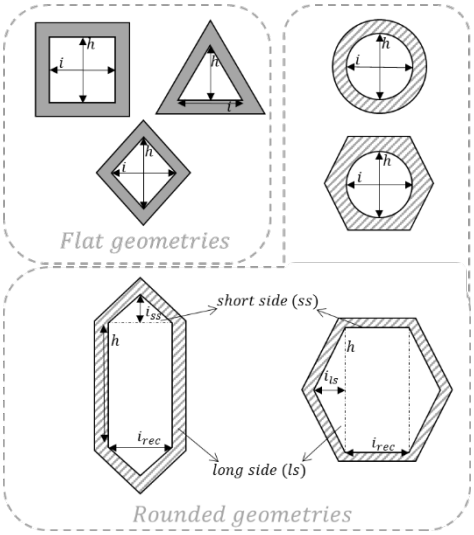

Figure 1: Geometries analysed. From left to right, from top to bottom: rectangular channel, triangular channel, hollow fiber, rhombic channel, hex-cir channel, hex-hex channel with $\alpha_{ss} > 0$ *and hex-hex channel with* $\alpha_{ls} > 0$.

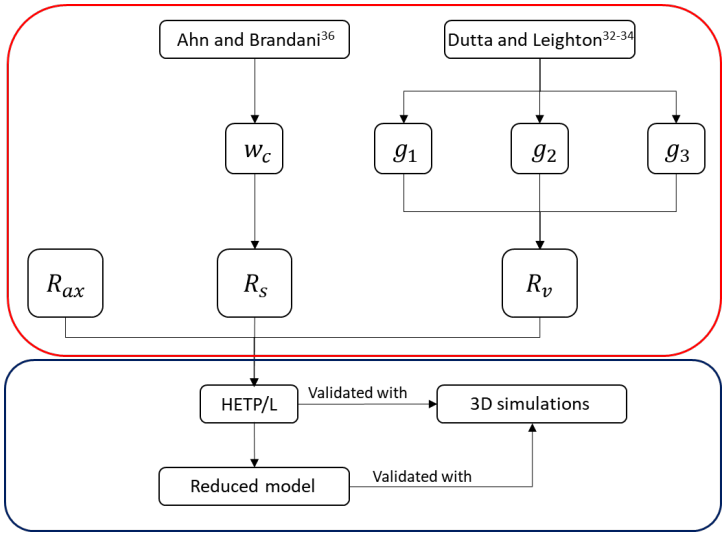

Figure 2: Schematic diagram of the procedure used to derive and validate the HETP equations for the different geometries and the reduced model. The procedure used to derive the HETP is highlighted in the red rectangle. The validation of the HETP equation is highlighted in the blue rectangle.

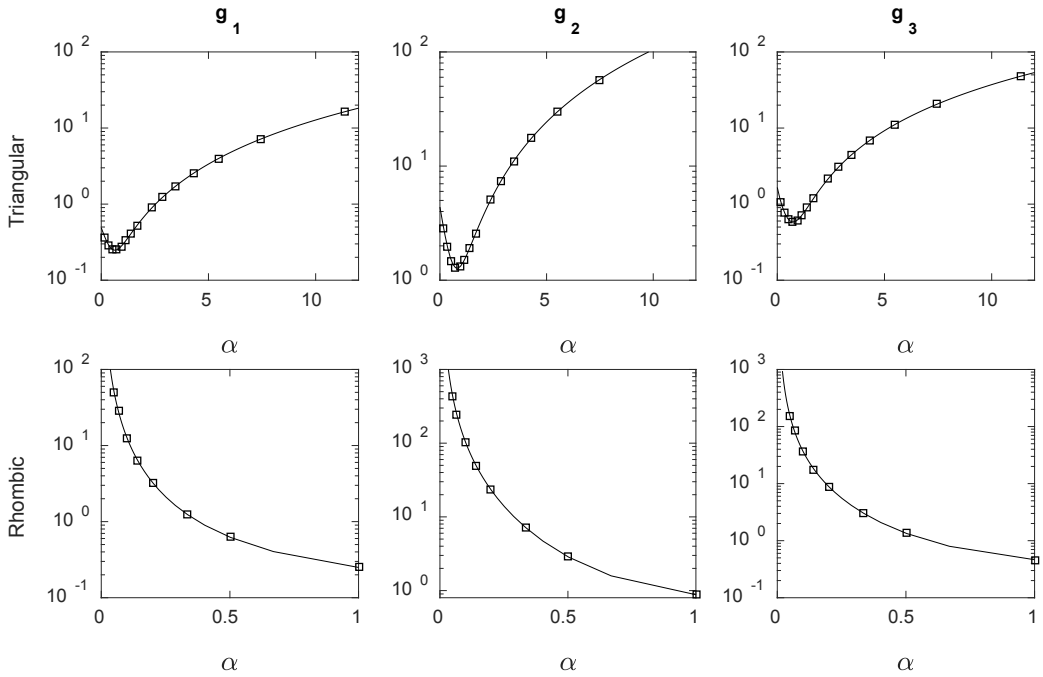

Figure 3: $g_i(\alpha)$ functions for the triangular and rhombic channel. Squares are numerical results and the solid line is the fitting correlation, eq.(8).

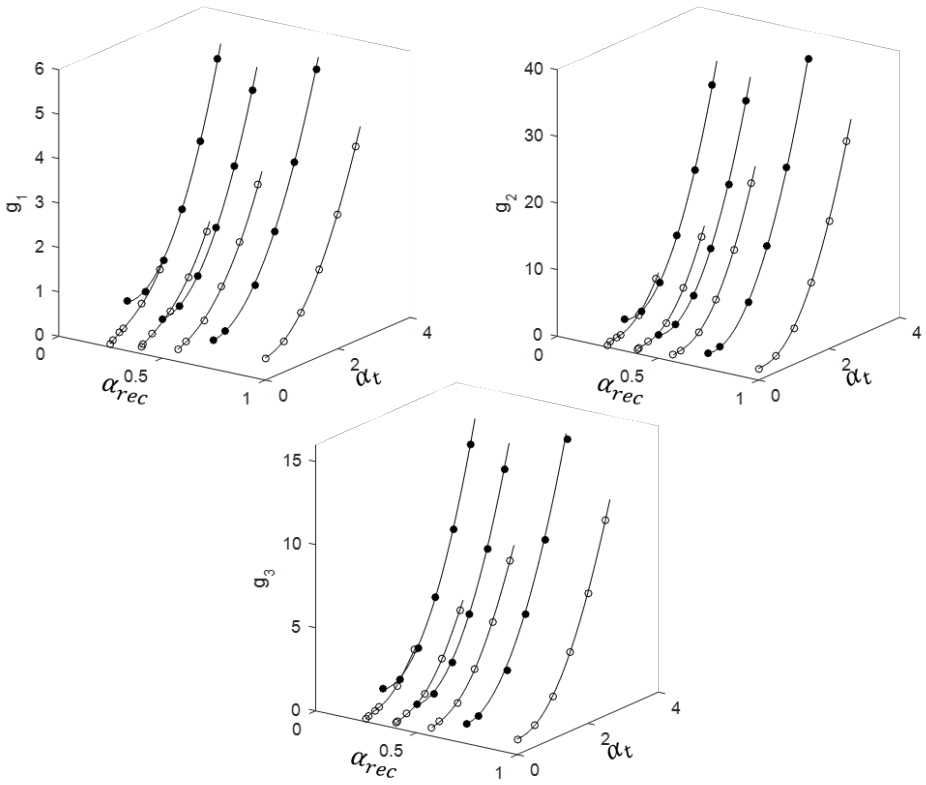

Figure 4:$g_i(\alpha)$ functions for the hex-hex channel. Solid lines are the fitted correlations while circles are the results from the numerical simulations: filled symbols for $\alpha_{ss} > 0$ and empty symbols for $\alpha_{ls} > 0$. On the y-axis $\alpha_t = \alpha_{ss}$ for $\alpha_{ss} > 0$ (filled circles), while $\alpha_t = \alpha_{ls}$ for $\alpha_{ls} > 0$ (empty circles).

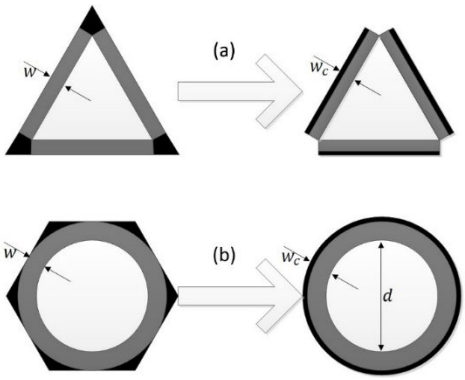

Figure 5: Redistribution of the solid for (a) triangular channel and (b) hex-cir channel.

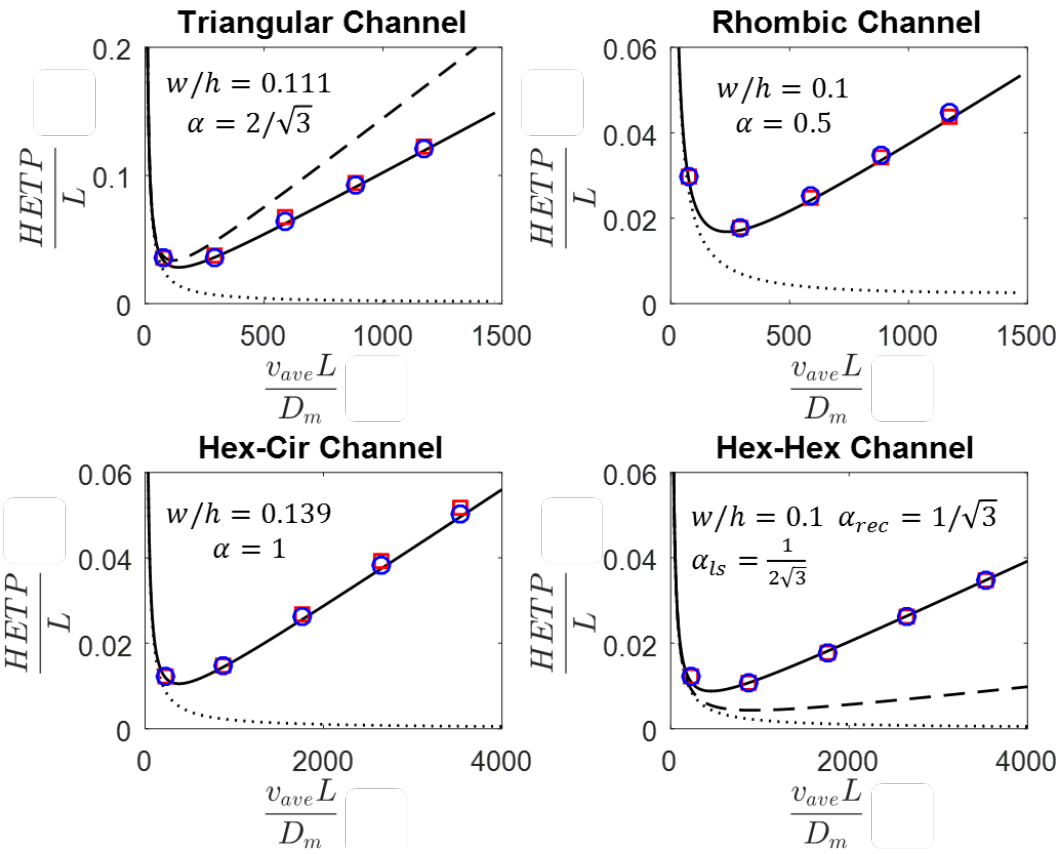

Figure 6: HETP plot for different geometries. Squares are 3D simulation results, and circles are simulation results using the reduced model. The dotted line is the fluid resistance only, the dashed line is the HETP calculated as in Patton et al.[35] (triangular and hex-hex geometries) and the solid line the HETP with corrected thickness.

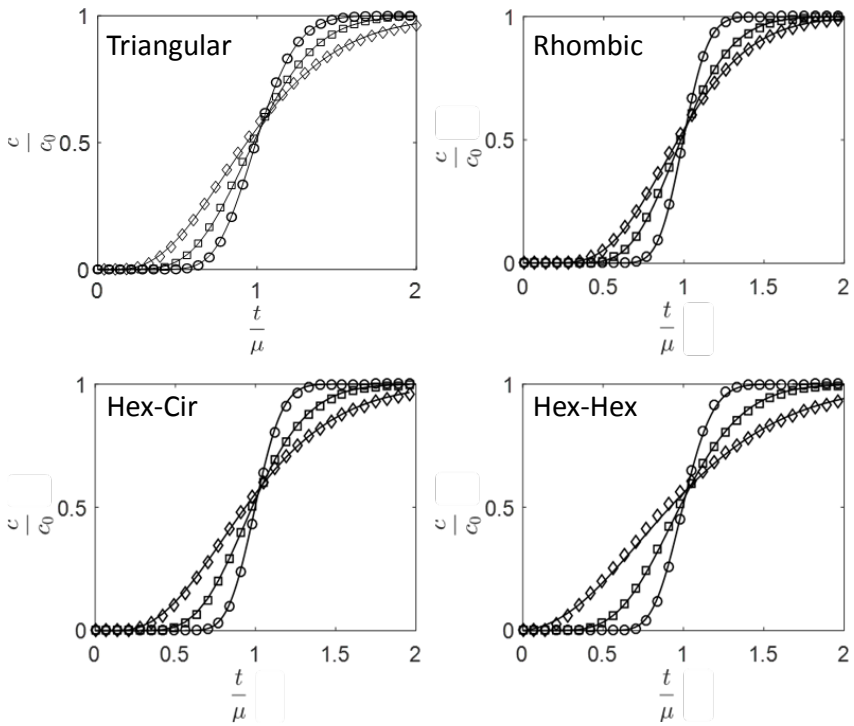

Figure 7: Comparison between 3D simulations (squares) and reduced order model (solid line). Geometrical parameters are the same as in Fig. 6.

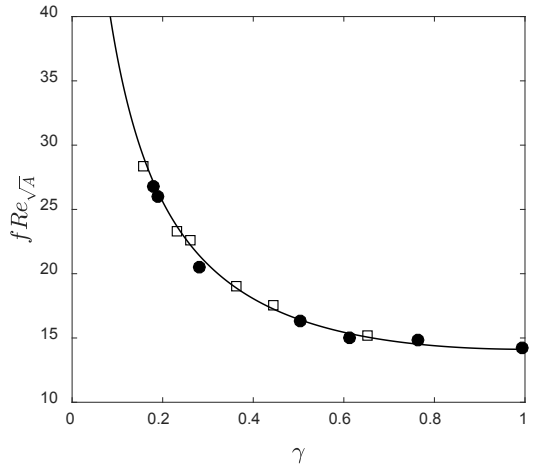

Figure 8: $fRe_{\sqrt{A}}$ correlation for hex-hex channel. Empty Squares are hex-hex channel with $\alpha_{ss} > 0$, filled circles hex-hex channel with $\alpha_{ls} > 0$ and solid line eq.(17) with γ calculated from the correlations in Table 4.

AIChE Journal

DOI10.1002/aic.17650

Table 1: Correlations for the corrected thickness of different geometries.

Triangle	$w_c = w + \frac{w^2}{2h}\left(1 + \frac{1}{\sin(\arctan(\alpha/2))}\right)$
Rhombus	$w_c = \frac{\left(1 + 2\frac{w/h}{\sin(atan(\alpha))}\right)\left(\alpha + 2\frac{w/h}{\sin(atan(\alpha^{-1}))}\right) - \alpha}{4\sqrt{1+\alpha^2}} h$
Hex-Cir	$w_c = \frac{\sqrt{\frac{4}{\pi}\left[\left(2\sqrt{3} - \pi\right)\frac{d^2}{4} + 2\sqrt{3}\, w(d+w)\right] + d^2} - d}{2}$
Rectangle[36]	$w_c = \frac{1 + \alpha + 2w/h}{2(\alpha + 1)} w$

Table 2: Derivation of the corrected thickness for the hex-hex channel

Steps	**Hex-Hex with $\alpha_{ls} > 0$**	**Hex-Hex with $\alpha_{ss} > 0$**
1	Calculate $A_{in} = (\alpha_{ls} + \alpha_{rec})h^2$ and $d = \sqrt{\frac{4A_{in}}{\pi}}$	Calculate $A_{in} = (1 + \alpha_{rec}\alpha_{ss})\alpha_{rec}h^2$ and $d = \sqrt{\frac{4A_{in}}{\pi}}$
2	Define $b = \frac{\alpha_{rec}h}{2} - 2\alpha_{ls}w\left[1 - \sqrt{1 + \left(\frac{1}{2\alpha_{ls}}\right)^2}\right]$ and $B = \frac{\alpha_{rec}h}{2} + 2\alpha_{ls}w\left[w\sqrt{1 + \left(\frac{1}{2\alpha_{ls}}\right)^2} + \frac{h}{2}\right]$	Define $b = h + 2w\left[\sqrt{1 + (2\alpha_{ss})^2} - 2\alpha_{ss}\right]$ and $B = h + 2h\left[\alpha_{rec}\alpha_{ss} + \frac{w}{h}\sqrt{1 + (2\alpha_{ss})^2}\right]$
3	Calculate $A_{out} = 2(b + B)\left(\frac{h}{2} + w\right)$	Calculate $A_{out} = (b + B)\left(\frac{\alpha_{rec}h}{2} + w\right)$
4	Calculate the corrected thickness as $w_c = \frac{\sqrt{\frac{4(A_{out} - A_{in})}{\pi} + d^2} - d}{2}$	

Table 3: Physical parameters for 3D simulations[36].

K (-)	40
D_m (m^2/s)	$1.7x10^{-5}$
D_s (m^2/s)	$7.4x10^{-10}$

Table 4: Correlations for the effective aspect ratio

Geometry	**Effective Aspect Ratio, γ**
Regular Polygons with $n_{sides} \in [4; \infty]$*	1
Triangle*	$[(2\alpha)^{0.53} + (2/\alpha)^{0.53}]^{-1/0.53}$
Rhombus*	$[(2\alpha)^{0.68} + (2/\alpha)^{0.68}]^{-1/0.68}$
Hex-Hex with $\alpha_{ss} = 0$	$\left[\left(\frac{\sqrt{3}}{2(\alpha_{rec} + \alpha_{ls})}\right)^{90} + \left(\frac{2(\alpha_{rec} + \alpha_{ls})}{\sqrt{3}}\right)^{90}\right]^{-1/95}$
Hex-Hex with $\alpha_{ls} = 0$	$\frac{1}{1/\alpha_{rec} + \alpha_{ss}}$

* From Duan and Yovanovich[48]

Table 5: Limits of the function $R\left(\frac{D_m}{\epsilon_p v R_p}, \frac{D_m}{KD_s}\right)$.

	$\lim_{\frac{D_m}{KD_s}\to 0^+} R\left(\frac{D_m}{\epsilon_p v R_p}, \frac{D_m}{KD_s}\right)$	$\lim_{\frac{D_m}{KD_s}\to \infty} R\left(\frac{D_m}{\epsilon_p v R_p}, \frac{D_m}{KD_s}\right)$
Triangular	601.28	94.39
Rectangular	1055	165.55
Rhombic	3341	524.6
Rounded	936	720